sciendo

Polish Journal of Chemical Technology, 26, 1, 16—23, 10.2478/pjct-2024-0003

Effect of calcination temperatures on optical and magnetic properties of $FeWO_4$ nanoparticles

Anh Q.K. Nguyen[1*], Thi K.N. Tran[1], Bich N. Hoang[1], Ngo T.C. Quyen[1], Tai T. Huynh[2], Nguyen P. Yen[3], Bich N. Nguyen[4*]

[1]Institute of Applied Technology and Sustainable Development, Nguyen Tat Thanh University, Ho Chi Minh City 70000, Viet Nam
[2]Ho Chi Minh City University of Natural Resources and Environment (HCMUNRE), Ho Chi Minh City 700000, Vietnam
[3]Youth Development Science and Technology Center, Ho Chi Minh City 70000, Viet Nam
[4]Dong Thap University, Cao Lanh City, 870000, Viet Nam
[*]*Corresponding author: e-mail:* nqkanh@ntt.edu.vn (Anh Q.K. Nguyen), nnbich@dthu.edu.vn (Bich N. Nguyen)

Calcination temperature is a crucial parameter that can be easily controlled to induce a change in material properties. Herein, iron tungstate ($FeWO_4$) was synthesized via a hydrothermal method using iron(II) sulfate heptahydrate and sodium tungstate dihydrate as precursors and calcined at the temperature between 300 °C and 700 °C. With increasing calcination temperature, the saturation magnetization of $FeWO_4$ nanoparticles decreased from 6.6 emu/g for $FeWO_4$ to 0.4 emu/g for $FeWO_4$_700, whereas their band gaps increased from 1.95 eV for $FeWO_4$ to 2.20 eV for $FeWO_4$_700. More crystallinity and crystal defects, and morphological changes at higher calcination temperatures contributed to varying magneto-optical properties of $FeWO_4$ nanoparticles.

Keywords: Iron tungstate; Calcination temperature; Optical; Magnetic; Hydrothermal synthesis.

INTRODUCTION

Iron tungstate ($FeWO_4$) is classified into ABO_4-type oxides, which possess a wolframite-type structure built up by WO_6 octahedral units[1]. Recently, $FeWO_4$ has been extensively applied to photocatalysis[2], electrocatalysis[3], biosensing[4], and memristive devices[5] owing to its low-cost production, strong chemical stability, and excellent electro-magneto-optical properties[6,7]. Therefore, several methods, such as hydrothermal[2], solvothermal[3], coprecipitation[8], sol-gel process[9], and chemical spray pyrolysis[5], have been developed for the synthesis of $FeWO_4$ nanoparticles. Among them, the hydrothermal method provides a simple and environmentally friendly means of preparing nanomaterials with controllable morphologies and phase structures, and desired physico-chemical characteristics via adjusting operating parameters[10]. In addition, the environment in the hydrothermal process facilitates the dissolution of reactant substances (i.e., even insoluble under normal conditions), resulting in homogenous nucleation and growth of nanocrystals; therefore, it has proven a particularly effective technique for the synthesis of bimetallic oxides, such as $FeWO_4$, with high purity[11].

Controlling synthetic parameters is an effective strategy for modifying the structural, morphological, and physicochemical properties of materials. $FeWO_4$ prepared at different pH exhibited different morphologies and band gap (E_g) values (i.e., hexagonal flakes and E_g = 2.35 eV at pH 2, small nanoparticles and E_g = 2.45 eV at pH 7, thin nanorods and E_g = 2.33 eV at pH 9, and a mixture of flakes, particles, and rods and E_g = 2.50 eV at pH 10)[12]. Increasing the amount of NaOH additive (0, 0.5, and 1 g) in the hydrothermal synthesis of $FeWO_4$ nanomaterials changed their morphologies from nanoparticles to nanorods to nanofibers with the increased BET surface areas of 4.4, 19.5, and 28.8 m^2/g, and the decreased charge transfer resistance, respectively[13]. Cetyltrimethylammonium bromide induced the formation of $FeWO_4$ nanowires with saturation magnetization (M_S) of 1.7 $emu \cdot g^{-1}$[14], while the combination of ethylenediaminetetraacetic acid disodium salt and hexamethylenetetramine directed the growth of flower-like $FeWO_4$ microcrystal with M_S of 0.01 $emu \cdot g^{-1}$[15].

Calcination temperature significantly affects the optical and magnetic characteristics of nanomaterials[16], and its effects are complex and various depending on the intrinsic nature of the materials. Calcination at elevated temperatures could induce crystal phase transformation, resulting in a difference in the optical properties of ZnO nanoparticles[17]. Increasing calcination temperature increased the crystallinity, reducing the band-gap values of CuO nanospheres due to the quantum confinement effect[18]. Hoghoghifard S. et al. reported that saturation magnetization of $NiFe_2O_4$ nanorods increased with increasing calcination temperature[19]; however, Chenari H.M. et al. showed an opposing result for $Cu_xCo_{3-x}O_4$[20]. These results could be attributed to the change of material surface, such as cation rearrangement, a varying amount of surface spins, and the formation of spin-glass states according to calcination temperature[21]. Therefore, the change in the magneto-optical behavior of various materials as a function of calcination temperature has been extensively investigated. While the influence of several synthetic parameters, such as pH and chemical additives, on the properties of $FeWO_4$ was explored, that of calcination temperature has not yet been reported.

In this work, we synthesized $FeWO_4$ nanoparticles via a hydrothermal route and calcined them at different temperatures. Crystal structure, morphology, surface area, magnetic, and optical properties of as-prepared $FeWO_4$ samples were entirely characterized using X-ray diffraction technique, transmission electron microscopy, gas sorption analyzer, vibrating sample magnetometer, and UV-Vis diffuse reflectance spectroscopy, respectively. The variation in saturation magnetization and band gap of $FeWO_4$ nanoparticles depending on calcination temperature was investigated and discussed in detail.

EXPERIMENTAL

Chemicals

Chemicals used in this study include: iron(II) sulfate heptahydrate ($FeSO_4 \cdot 7H_2O$, ≥99%, Xilong), sodium tungstate dihydrate ($Na_2WO_4 \cdot 2H_2O$, ≥99%, Acros), sodium hydroxide (NaOH, ≥96%, Xilong), barium sulfate ($BaSO_4$, ≥99%, Xilong). Deionized water was produced by a water still (WSC/4D, Hamilton Laboratory Glass LTD., UK).

Synthetic procedure of $FeWO_4$ nanoparticles

$FeWO_4$ nanoparticles were fabricated via a hydrothermal method using $Na_2WO_4 \cdot 2H_2O$ and $FeSO_4 \cdot 7H_2O$ as precursors of W and Fe, respectively (Fig. 1)[12]. 35 mL of Na_2WO_4 solution (5 mmol, 1.6493 g) was pipetted dropwise into a 100 mL-beaker containing 35 mL of $FeSO_4$ solution (5 mmol, 1.3901 g) under vigorous stirring at 700 rpm. The mixture was adjusted to pH 8 before being transferred to a 100 mL-sealed teflon vessel autoclave and heated at 200 °C for 12 h in an oven (UN10, Memmert, Germany). The precipitate was separated via centrifugation and washed several times with D.I. H_2O before being dried at 80 °C for 12 h. The mass of the obtained product and the synthetic yield were 0.918 ± 0.017 g and 60.43 ± 1.15 %, respectively. Finally, the samples were calcined at different temperatures for 3 h to compare their properties. $FeWO_4$, $FeWO_4$_300, $FeWO_4$_500, and $FeWO_4$_700 denote the sample without calcination and samples calcined at 300, 500, and 700°C, respectively (Fig. 2).

Characterization methods

Crystal structures of the prepared materials were determined using an X-ray diffractometer (Empyrean, PANalytical). XRD patterns were recorded at the voltage of 45 kV and current of 40 mA using Cu anode (Kα = 1.54 Å) in the 2θ range of 5−80° with a scanning rate of 1.6°/min. Morphologies of $FeWO_4$ samples were observed on a transmission electron microscope (JEM 1400 flash, JEOL) operating at 120 kV. The existence of chemical elements on the surface of $FeWO_4$ samples was identified using a scanning electron microscope (S4800, Hitachi) coupled with an energy-dispersive X-ray (EDX) spectroscopy (H-7593, HORIBA). The particle size analysis was performed on a nanopartical series

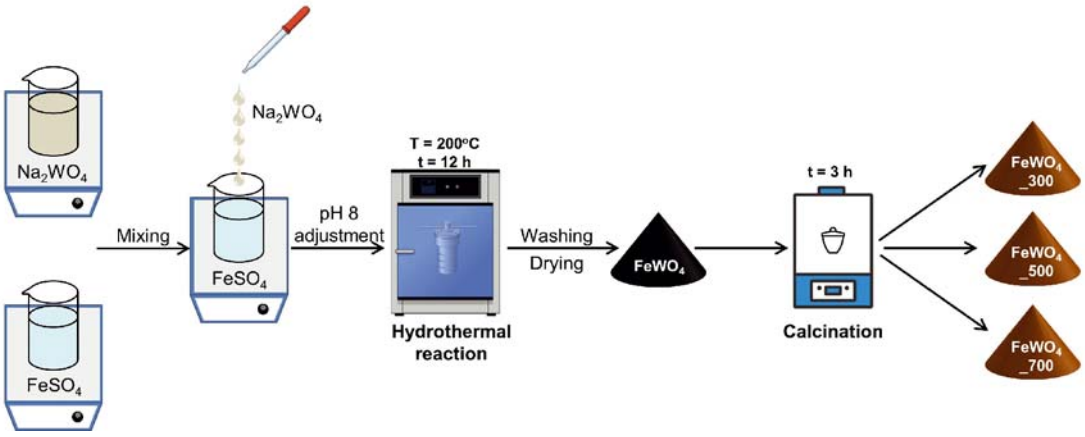

Figure 1. Scheme for synthetic procedure of $FeWO_4$ nanoparticles

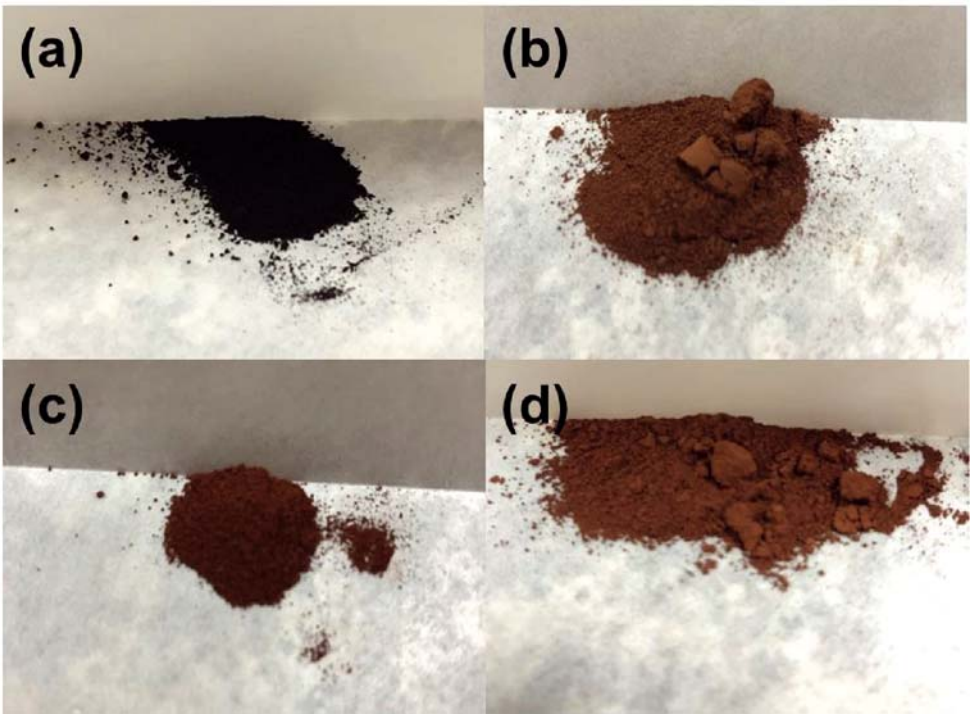

Figure 2. Pictures of (a) $FeWO_4$, (b) $FeWO_4$_300, (c) $FeWO_4$_500, and (d) $FeWO_4$_700 samples

instrument (SZ-100, HORIBA). The chemical bonds in $FeWO_4$ samples were determined using a Fourier-transform infrared spectroscopy (FT-IR) (NICOLET 6700, Thermo). Nitrogen sorption isotherms of $FeWO_4$ samples were measured using a gas sorption analyzer (Nova 4000e, Quantachrome Instruments) and employed to calculate surface area values and pore size distribution based on Brunauer-Emmett-Teller (BET) and Barrett-Joyner-Halenda (BJH) methods, respectively. Magnetization curves of $FeWO_4$ samples were measured using a vibrating sample magnetometer (Institute of Materials Science, Vietnam). The diffuse reflectance UV–Vis absorption spectra of $FeWO_4$ samples were recorded on a UV–Vis spectrophotometer (UV-2600, Shimadzu) using $BaSO_4$ as the reference. The optical band gap energies were estimated by extrapolating the linear segment of the Tauc plot to the x-axis.

RESULTS AND DISCUSSION

The XRD pattern of $FeWO_4$ exhibits the diffraction peaks at 2θ = 18.8, 23.7, 24.4, 30.4, 36.2, 36.3, 38.1, 41.1, 51.8, 53.5, 61.5, and 64.1, which are attributed to (100), (011), (110), (111), (002), (021), (200), (121), (130), (202), (113), and (132) crystal planes of monoclinic $FeWO_4$ (JCPDS 74-1130), respectively (Fig. 3)[12]. When calcined at 300−700 °C, the above characteristic peaks became sharper, particularly for $FeWO_4$_700, without additional impurity peaks, indicating that the calcination process did not change the structural phase, but increased the crystallinity. In addition, a slight shift of the crystalline peaks to higher angles was observed with increasing calcination temperature, which implies a decrease in lattice spacing and distortion in the crystal structure, possibly because of the formation of lattice defects and/or oxygen vacancies at high temperatures[22]. High temperature during calcination could rupture and rearrange the bonding in the lattice or on the surface and increase the growth rate of particles, which induced to generate crystal defects[23–25].

The distinctive bonds of $FeWO_4$ were observed in their FT-IR spectra (Fig. 4). The peaks at 3420 and 1622 cm^{-1} belong to the −OH stretching and bending vibration of water molecules, respectively[9]. The bands located at 871

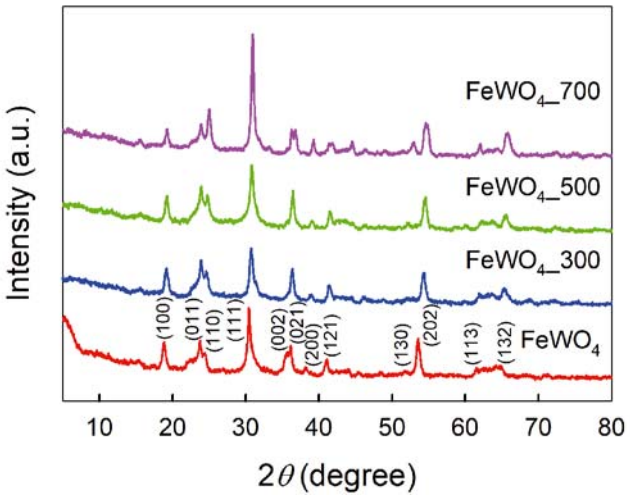

Figure 3. XRD patterns of various $FeWO_4$ nanoparticles

and 825 cm^{-1} can be attributed to the symmetrical stretching modes of Fe−O−W[26]. The W−O bond stretching in WO_6 octahedral appeared at a wavenumber of 705 cm^{-1}[26]. The peak shifts toward higher wavenumbers in the FT-IR spectra of $FeWO_4$_300, $FeWO_4$_500, and $FeWO_4$_700 were noticed, suggesting a progressive reduction in bond lengths with calcination temperature increment[27], which is in good agreement with the XRD results.

TEM images in Figure 5 display the morphologies of $FeWO_4$ samples treated at different calcination temperatures. $FeWO_4$ samples synthesized with and without calcination comprise the mixture of nanosphere (i.e., diameter ~ 13−70 nm) and nanorod (i.e., width ~ 6−50 nm and length ~ 45−400 nm). The nanorod lengths of $FeWO_4$_700 shortened compared with those of other $FeWO_4$ because higher calcination temperature may accelerate the chaotic state of particles, which inhibits a crystal orientation along to a specific plane and reduces the length of nanorods[19, 28]. Figure 6 shows SEM micrographs and EDX analyses of various $FeWO_4$ samples. Several large aggregation of rod and sphere particles was observed on the surface of all $FeWO_4$ samples. The presence of iron, tungsten, and oxygen in all $FeWO_4$ samples was verified by the EDX spectra, confirming the formation of $FeWO_4$ without impurities. Figure 7 shows the particle size distribution of $FeWO_4$

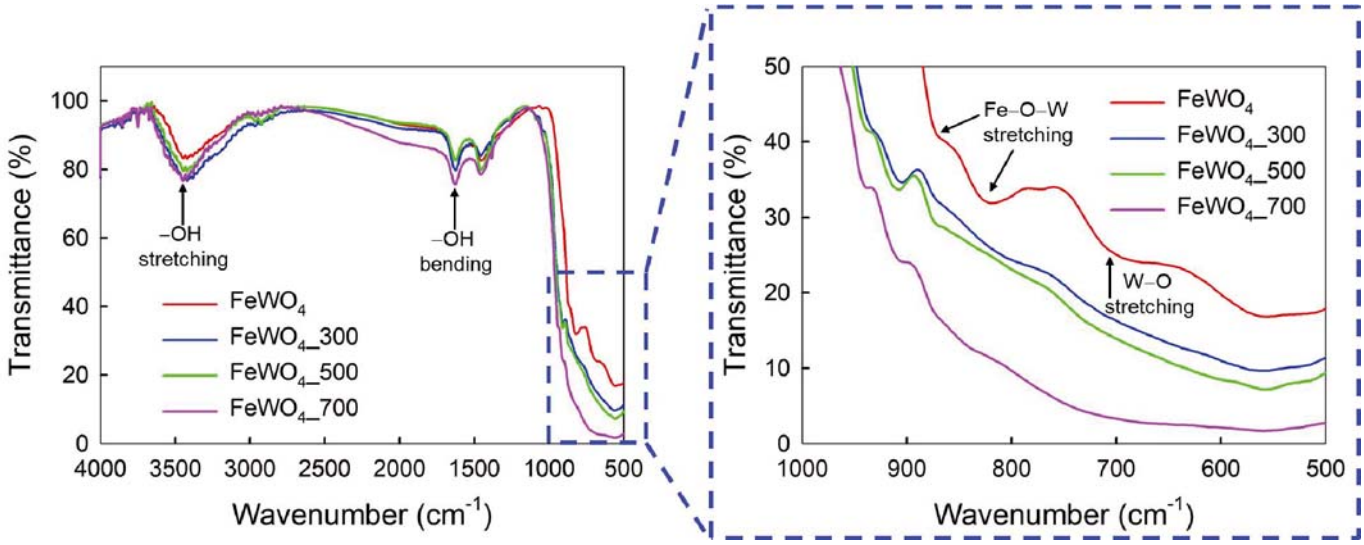

Figure 4. FT-IR spectra of $FeWO_4$ nanoparticles

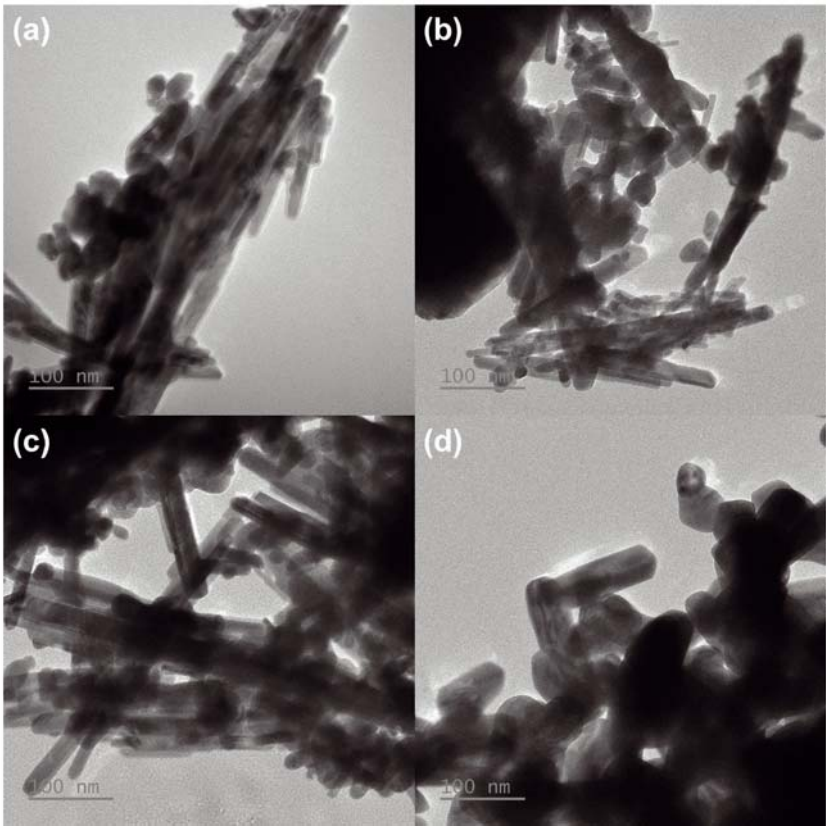

Figure 5. TEM images of (a) $FeWO_4$, (b) $FeWO_4$_300, (c) $FeWO_4$_500, and (d) $FeWO_4$_700

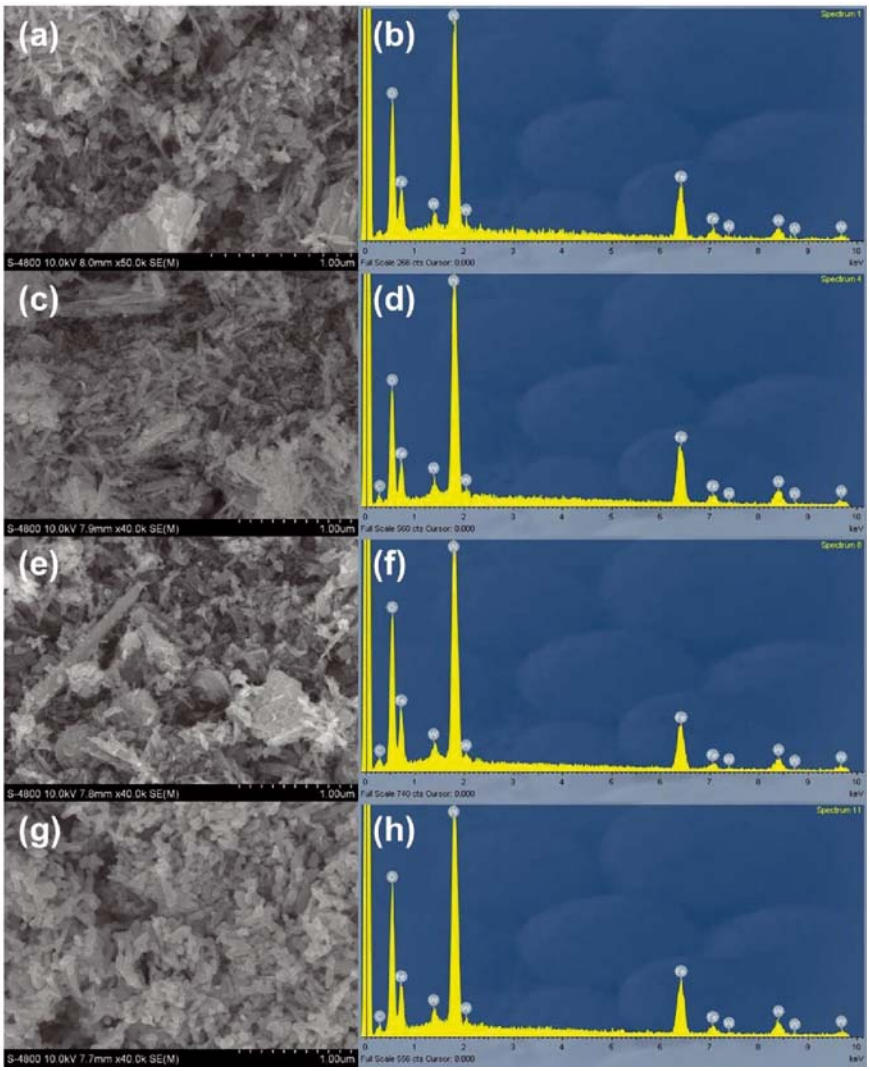

Figure 6. SEM images and EDX analyses of (a) and (b) $FeWO_4$, (c) and (d) $FeWO_4$_300, (e) and (f) $FeWO_4$_500, and (g) and (h) $FeWO_4$_700

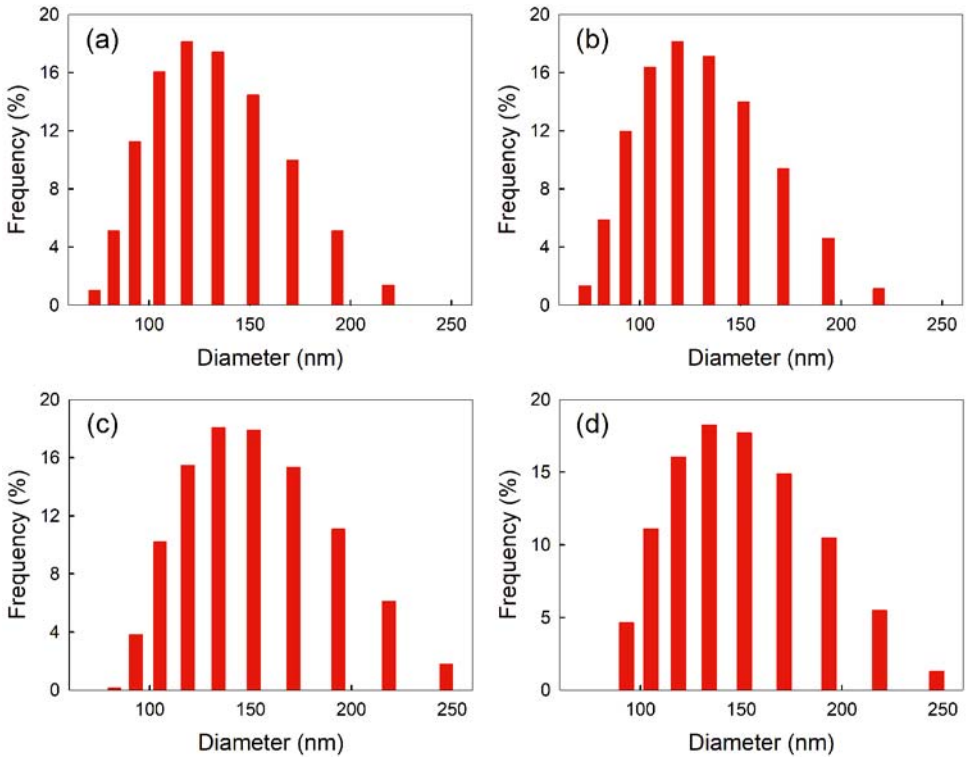

Figure 7. Particle size distribution of (a) $FeWO_4$, (b) $FeWO_4$_300, (c) $FeWO_4$_500, and (d) $FeWO_4$_700

samples measured by using dynamic light scattering technique. Their particle size distributed in the range of 72.9−247.0 nm with average diameters calculated as 121.6, 119.9, 140.8, and 138.8 nm for $FeWO_4$, $FeWO_4$_300, $FeWO_4$_500, and $FeWO_4$_700, respectively.

N_2 sorption curves of all $FeWO_4$ samples in Figure 8a are identical to the type IV isotherm associated with the H3 hysteresis loop based on the IUPAC recommendation[29], suggesting the existence of mesoporosity in their structures[30]. The Brunauer-Emmett-Teller (BET) surface area and Barrett-Joyner-Halenda (BJH) pore volume values were calculated to be 34.8 m^2/g and 0.223 cm^3/g for $FeWO_4$, 30.5 m^2/g and 0.201 cm^3/g for $FeWO_4$_300, 27.4 m^2/g and 0.192 cm^3/g for $FeWO_4$_500, and 10.8 m^2/g and 0.045 cm^3/g for $FeWO_4$_700, respectively (Table 1). The decrease in surface areas and pore volumes with increasing calcination temperature is due to disruption and obstruction of the pore structure at high temperatures[31]. The pore size distribution of $FeWO_4$ materials was derived from the adsorption isotherm based on the BJH method (Fig. 8b). The narrow peaks at 2.181 nm for $FeWO_4$, 2.207 nm for $FeWO_4$_300, 2.571 nm for $FeWO_4$_500, and 0.996 nm for $FeWO_4$_700 can be attributed to intraparticle pores, while the broad peaks at 33.454 nm for $FeWO_4$, 34.464 nm for $FeWO_4$_300, and 34.160 nm for $FeWO_4$_500 can be assigned to interparticle voids[32,33]. The broad peak in the pore size distribution of $FeWO_4$_700 disappeared due to the formation of large aggregates at high temperatures.

Table 1. BET surface area, BJH pore volume, and pore diameter values of various $FeWO_4$ samples

Sample	BET surface area (m^2/g)	BJH pore volume (cm^3/g)	Pore diameter (nm)
$FeWO_4$	34.811	0.223	2.181
$FeWO_4$_300	30.464	0.201	2.207
$FeWO_4$_500	27.381	0.192	2.571
$FeWO_4$_700	10.766	0.045	0.996

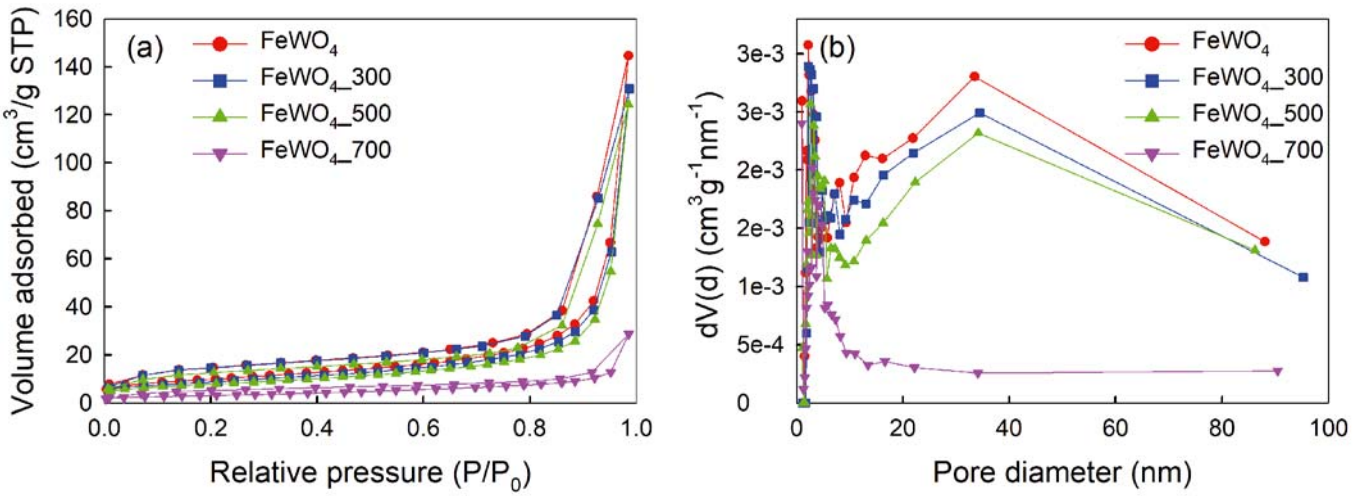

Figure 8. (a) Nitrogen sorption isotherms and (b) pore size distribution of various $FeWO_4$ samples

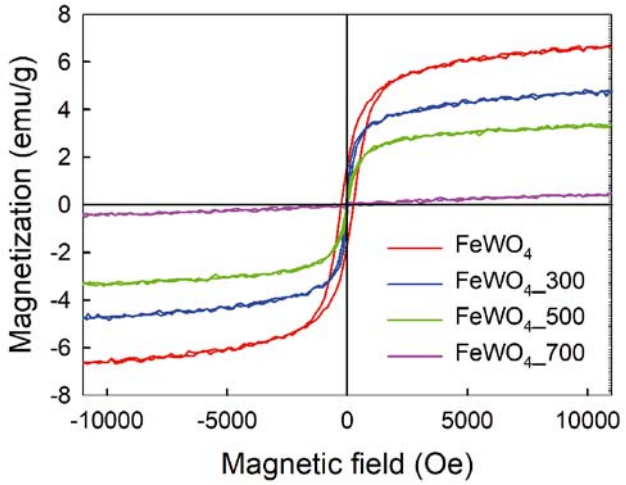

Figure 9. Magnetization curves of various $FeWO_4$ nanoparticles

The effects of calcination temperatures on the magnetic properties of $FeWO_4$ nanoparticles were investigated (Fig. 9). $FeWO_4$ materials showed similar hysteresis loops when the external magnetic field was applied and removed, indicating their ferromagnetic property under room temperature. The saturation magnetization, coercivity, and retentivity of $FeWO_4$ materials were derived from their hysteresis loops and presented in Table 2. All three above parameters of $FeWO_4$ samples decreased with an increase in calcination temperature, suggesting that calcination had a negative impact on their magnetic flux density and retentivity. These results could be attributed to the defect formation and morphological changes of $FeWO_4$ samples observed in the XRD patterns and TEM images depending on calcination temperatures. In addition, low specific surface area caused by severe aggregation at high calcination temperature reduced the amount of surface spins[34], which negatively affected the magnetic properties of $FeWO_4$ materials. $FeWO_4$ nanoparticles with higher saturation magnetization may be more appealing to applications in catalysis and biomedicine.

The optical band gap energies, which were derived from the Tauc plots of $FeWO_4$, $FeWO_4$_300, $FeWO_4$_500, and $FeWO_4$_700 (Fig. 10a), are 1.95, 2.00, 2.05, and 2.20 eV, respectively. All $FeWO_4$ samples can absorb visible light region ($\lambda > 420$ nm) (Fig. 10b); however, $FeWO_4$_700 exhibits a larger band gap than the others, which may decelerate the recombination of photo-generated electrons and holes for enhancing photocatalysis efficiency[35].

Table 2. Magnetic properties of various $FeWO_4$ nanoparticles

Type	Saturation magnetization[a] (emu/g)	Coercivity[b] (Oe)	Retentivity[c] (emu/g)
$FeWO_4$	6.6	257.5	1.63
$FeWO_4$_300	4.8	38.0	0.41
$FeWO_4$_500	3.3	20.7	0.14
$FeWO_4$_700	0.4	n.d.[d]	0.04

[a] Magnetization value at the highest magnetic field.
[b] Magnetic field at the intersection point between the hysteresis loop and negative x-axis.
[c] Magnetization value at the intersection point between the hysteresis loop and positive y-axis.
[d] Not determined due to many intersection points caused by noise.

More crystallinity and oxygen vacancy content in $FeWO_4$ nanoparticles at higher calcination temperatures could be responsible for the increase in their band gap values[36].

Table 3 shows a comparison of morphology, BET surface areas, band-gap, and saturation magnetization of $FeWO_4$ prepared in this study with other works. Among synthetic methods, hydrothermal was employed for the synthesis of $FeWO_4$ the most, and allowed producing the $FeWO_4$ materials with various morphologies. BET, band-gap, and saturation magnetization values of $FeWO_4$ prepared in previous studies varied in the range of 3.33−33.35, 1.54−3.17, and 0.03−14.7, respectively, which are almost comparable to those of $FeWO_4$ prepared in this study. This result suggests that changing calcination temperatures effectively controlled the physical properties of the $FeWO_4$ material. In addition, this study provided information on both magnetic and optical properties and their relationship with calcination temperature, which was absent from other studies.

CONCLUSION

$FeWO_4$ nanoparticles were successfully synthesized via a hydrothermal reaction of Na_2WO_4 and $FeSO_4$ at 200 °C for 12 h. The calcination process increased crystallinity, distorted the lattice spacing, facilitated the defects formation, and hindered the anisotropic crystal growth, which altered the properties of $FeWO_4$ nanoparticles, including surface areas, magnetism, and band gap energies. When increasing calcination temperature, the optical band gap of $FeWO_4$ samples broadened from 1.95 eV to 2.20 eV, but their saturation magnetization values reduced from 6.6 emu/g to 0.4 emu/g. Manipulating calcination temperature is a facile and effective way, enabling $FeWO_4$

Table 3. Physical properties of $FeWO_4$ in this study compared with previous publications

No.	Synthetic method	Morphology	BET value (m^2/g)	Optical band-gap (eV)	Magnetization (emu/g)	Ref.
1	solvothermal	platelike	n.d.[a]	n.d.	0.5 at 100 K	37
2	hydrothermal	nanoparticle	22.17	1.54	0.51	38
3	hydrothermal	nanorod	23.30	1.98	n.d.	39
4	hydrothermal	quadrilateral disk	15.00	1.98	n.d.	40
5	hydrothermal	nanorod	33.35	2.50	n.d.	41
6	hydrothermal	nanoparticle	21.75	1.95	n.d.	42
7	hydrothermal	nanorod	n.d.	2.16	0.03 at 100 K	43
8	hydrothermal	irregular block	3.33	2.79	n.d.	44
9	hydrothermal	sphere	n.d.	n.d.	14.7	45
10	solvothermal	flowerlike	30.77	1.70	n.d.	46
11	co-precipitation	rod	17.76	1.95	n.d.	47
12	hydrothermal	nanowire	n.d.	n.d.	1.7	14
13	hydrothermal	nanocrystal	n.d.	n.d.	1.0 at 100 K	48
14	sol-gel	irregular block	36.58	3.17	n.d.	9
15	hydrothermal	nanosphere + nanorod	10.77–34.81	1.95–2.20	0.4–6.6	This study

[a] Not determined

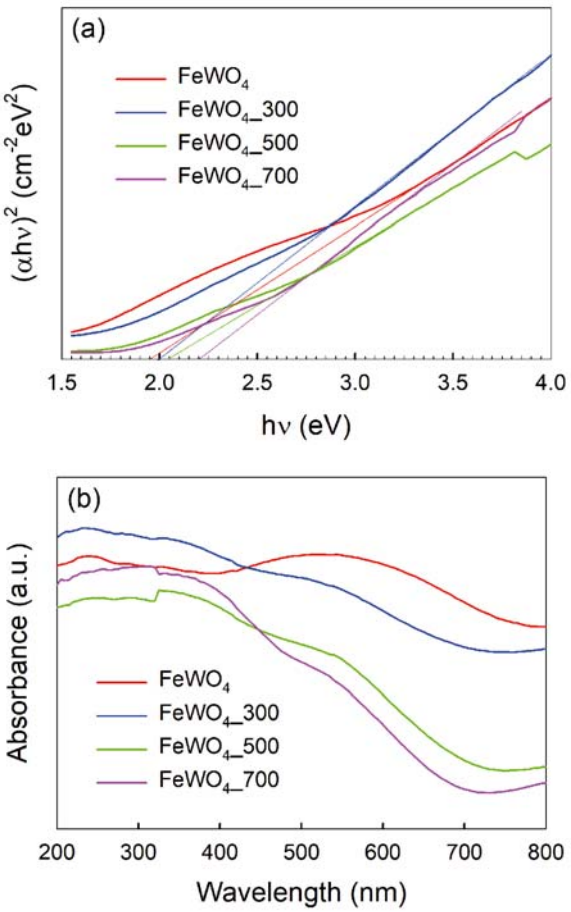

Figure 10. (a) Tauc plots and (b) UV–visible absorption spectra of various $FeWO_4$ nanoparticles

nanoparticles with various physicochemical properties to be applicable to a wide range of practical fields.

ACKNOWLEDGEMENT

The research topic was supported by The Youth Incubator for Science and Technology Programme, managed by Youth Promotion Science and Technology Center - Ho Chi Minh Communist Youth Union and Department of Science and Technology of Ho Chi Minh City, the contract number is "17/2022/ HĐ-KHCNT-VU" signed on 30th, December, 2022.

LITERATURE CITED

1. Sorouri, A.M., Sobhani-Nasab, A., Ganjali, M.R., Manani, S., Ehrlich, H., Joseph, Y. & Rahimi-Nasrabadi, M. (2023). Metal tungstates nanostructures for supercapacitors: A review. *Appl. Mater. Today* 32, 101819. DOI: 10.1016/j.apmt.2023.101819.

2. Qian, J., Shen, L., Wang, Y., Li, L. & Zhang, Y. (2023). Photo-Fenton catalytic and photocatalytic performance of $FeWO_4$ nanorods prepared at different pH. *Mater. Lett.* 334, 133705. DOI: 10.1016/j.matlet.2022.133705.

3. Adak, M.K., Rajput, A., Mallick, L. & Chakraborty, B. (2022). Electrochemically robust ferberite ($FeWO_4$) nanostructure as an anode material for alkaline water- and alcohol--oxidation reaction. *ACS Appl. Energ. Mater.* 5(5), 5652–5665. DOI: 10.1021/acsaem.1c03995.

4. Tang, X., Chen, J., Zhang, M., Sun, J. & Yang, X. (2023). Tunable catalytic activity of $FeWO_4$ nanomaterials for sensitive assays of pyrophosphate ion and alkaline phosphatase activity. *Sci. China Chem.* 66(6), 1860–1868. DOI: 10.1007/s11426-023-1583-8.

5. Patil, A.R., Dongale, T.D., Namade, L.D., Mohite, S.V., Kim, Y., Sutar, S.S., Kamat, R.K. & Rajpure, K.Y. (2023). Sprayed $FeWO_4$ thin film-based memristive device with negative differential resistance effect for non-volatile memory and synaptic learning applications. *J. Colloid Interf. Sci.* 642, 540–553. DOI: 10.1016/j.jcis.2023.03.189.

6. Qian, H., Cao, L., Liao, S., Xie, S., Xiong, X. & Zou, J. (2023). Construction of noble-metal-free $FeWO_4/Mn_{0.5}Cd_{0.5}S$ photocatalyst to optimize H_2 evolution performance in water splitting. *Int. J. Hydrog. Energy* 48(23), 8514–8525. DOI: 10.1016/j.ijhydene.2022.11.284.

7. Wang, H., Xu, L., Deng, D., Liu, X., Li, H. & Su, D. (2023). Regulated electronic structure and improved electrocatalytic performances of S-doped $FeWO_4$ for rechargeable zinc-air batteries. *J. Energy Chem.* 76, 359–367. DOI: 10.1016/j.jechem.2022.09.023.

8. Goubard-Bretesché, N., Crosnier, O., Douard, C., Iadecola, A., Retoux, R., Payen, C., Doublet, M.-L., Kisu, K., Iwama, E., Naoi, K., Favier, F. & Brousse, T. (2020). Unveiling pseudocapacitive charge storage behavior in $FeWO_4$ electrode material by operando X-ray absorption spectroscopy. *Small* 16(33), 2002855. DOI: 10.1002/smll.202002855.

9. Boudghene Stambouli, H., Guenfoud, F., Benomara, A., Mokhtari, M. & Sönmez-Çelebi, M. (2021). Synthesis of $FeWO_4$ heterogeneous composite by the sol–gel process: enhanced photocatalytic activity on malachite green. *React. Kinet. Mech. Catal.* 133(1), 563–578. DOI: 10.1007/s11144-021-01994-x.

10. Yang, G. & Park, S.-J. (2019). Conventional and microwave hydrothermal synthesis and application of functional materials: a review. *Materials* 12(7), 1177. DOI: 10.3390/ma12071177.

11. Patil, S.S., Chougale, U.M., Kambale, R.K. & Fulari, V.J. (2023). Hydrothermal synthesis of $CoWO_4$ nanoparticles and evaluation of their supercapacitive performance. *J. Energy Storage* 67, 107517. DOI: 10.1016/j.est.2023.107517.

12. Yu, F., Cao, L., Huang, J. & Wu, J. (2013). Effects of pH on the microstructures and optical property of $FeWO_4$ nanocrystallites prepared via hydrothermal method. *Ceram. Int.* 39(4), 4133–4138. DOI: 10.1016/j.ceramint.2012.10.269.

13. Sun, D., Iqbal, N., Liao, W., Lu, Y., He, X., Wang, K., Ma, B., Zhu, Y., Sun, K., Sun, Z. & Li, T. (2022). Efficient degradation of MB dye by 1D $FeWO_4$ nanomaterials through the synergistic effect of piezo-Fenton catalysis. *Ceram. Int.* 48(17), 25465–25473. DOI: 10.1016/j.ceramint.2022.05.225.

14. Sun, B., Liu, Y. & Chen, P. (2014). Room-temperature multiferroic properties of single-crystalline FeWO4 nanowires. *Scr. Mater.* 89, 17–20. DOI: 10.1016/j.scriptamat.2014.06.030.

15. Zhang, J., Wang, Y., Li, S., Wang, X., Huang, F., Xie, A. & Shen, Y. (2011). Controlled synthesis, growth mechanism and optical properties of $FeWO_4$ hierarchical microstructures. *Cryst. Eng. Comm.* 13(19), 5744–5750. DOI: 10.1039/C1CE05416C.

16. Kądziołka, D., Grzechulska-Damszel, J. & Schmidt, B. (2022). Simultaneous photooxidation and photoreduction of phenol and Cr(VI) ions using titania modified with nanosilica. *Pol. J. Chem. Technol.* 24(4), 23–29. DOI: 10.2478/pjct-2022-0025.

17. Sangeetha, A., Jaya Seeli, S., Bhuvana, K.P., Kader, M.A. & Nayak, S.K. (2019). Correlation between calcination temperature and optical parameter of zinc oxide (ZnO) nanoparticles. *J. Sol-Gel Sci. Technol.* 91(2), 261–272. DOI: 10.1007/s10971-019-05000-8.

18. Chan, Y.B., Selvanathan, V., Tey, L.-H., Akhtaruzzaman, M., Anur, F.H., Djearamane, S., Watanabe, A. & Aminuzzaman, M. (2022). Effect of calcination temperature on structural, morphological and optical properties of copper oxide nanostructures derived from Garcinia mangostana L. leaf extract. *Nanomaterials* 12(20), 3589. DOI: 10.3390/nano12203589.

19. Hoghoghifard, S. & Moradi, M. (2022). Influence of annealing temperature on structural, magnetic, and dielectric properties of $NiFe_2O_4$ nanorods synthesized by simple hy-

drothermal method. *Ceram. Int.* 48(12), 17768–17775. DOI: 10.1016/j.ceramint.2022.03.047.

20. Mahmoudi Chenari, H. & Zarodi, M. (2022). Electrospinning process of $Cu_xCo_{3-x}O_4$ fibers (CCOFs): structural, surface morphology, optical and magnetic study. *J. Magn. Magn. Mater.* 562, 169853. DOI: 10.1016/j.jmmm.2022.169853.

21. Victory, M., Pant, R.P. & Phanjoubam, S. (2020). Synthesis and characterization of oleic acid coated Fe–Mn ferrite based ferrofluid. *Mater. Chem. Phys.* 240, 122210. DOI: 10.1016/j.matchemphys.2019.122210.

22. Shen, H., Xue, W., Fu, F., Sun, J., Zhen, Y., Wang, D., Shao, B. & Tang, J. (2018). Efficient degradation of phenol and 4-nitrophenol by surface oxygen vacancies and plasmonic silver co-modified Bi_2MoO_6 photocatalysts. *Chem.-Eur. J.* 24(69), 18463–18478. DOI: 10.1002/chem.201804267.

23. Liu, D., Lv, Y., Zhang, M., Liu, Y., Zhu, Y., Zong, R. & Zhu, Y. (2014). Defect-related photoluminescence and photocatalytic properties of porous ZnO nanosheets. *J. Mater. Chem. A* 2(37), 15377–15388. DOI: 10.1039/C4TA02678K.

24. Nandi, P. & Das, D. (2019). Photocatalytic degradation of Rhodamine-B dye by stable ZnO nanostructures with different calcination temperature induced defects. *J. Appl. Surf. Sci.* 465, 546–556. DOI: 10.1016/j.apsusc.2018.09.193.

25. Teh, G.B., Wong, Y.C. & Tilley, R.D. (2011). Effect of annealing temperature on the structural, photoluminescence and magnetic properties of sol–gel derived Magnetoplumbite-type (M-type) hexagonal strontium ferrite. *J. Magn. Magn. Mater.* 323(17), 2318–2322. DOI: 10.1016/j.jmmm.2011.04.014.

26. Rashidizadeh, A., Esmaili Zand, H.R., Ghafuri, H. & Rezazadeh, Z. (2020). Graphitic carbon nitride nanosheet/$FeWO_4$ nanoparticle composite for tandem photooxidation/knoevenagel condensation. *ACS Appl. Nano Mater.* 3(7), 7057–7065. DOI: 10.1021/acsanm.0c01380.

27. Jamali, M. & Shariatmadar Tehrani, F. (2020). Effect of synthesis route on the structural and morphological properties of WO_3 nanostructures. *Mater. Sci. Semicond. Process* 107, 104829. DOI: 10.1016/j.mssp.2019.104829.

28. Leal, G.F., Barrett, D.H., Carrer, H., Figueroa, S.J.A., Teixeira-Neto, E., Curvelo, A.A.S. & Rodella, C.B. (2019). Morphological, structural, and chemical properties of thermally stable Ni-Nb_2O_5 for catalytic applications. *J. Phys. Chem. C* 123(5), 3130–3143. DOI: 10.1021/acs.jpcc.8b09177.

29. Thommes, M., Kaneko, K., Neimark, A.V., Olivier, J.P., Rodriguez-Reinoso, F., Rouquerol, J. & Sing, K.S.W. (2015). Physisorption of gases, with special reference to the evaluation of surface area and pore size distribution (IUPAC Technical Report). *Pure Appl. Chem.* 87(9-10), 1051–1069. DOI: 10.1515/pac-2014-1117.

30. Tran, N.M., Doan, T.C. & Yoo, H. (2022). Fabrication of hollow fibrous nanosilica with large pore channels. *Chem. Commun.* 58(89), 12431–12434. DOI: 10.1039/D2CC04680F.

31. Prates da Costa, E., Hofmann, A., Göbel, U., Cop, P. & Smarsly, B.M. (2022). Development of pore morphology during nitrate group removal by calcination of mesoporous $Ce_xZr_{1-x-y-z}Y_yLa_zO_{2-\delta}$ Powders. *Langmuir* 38(27), 8342–8352. DOI: 10.1021/acs.langmuir.2c00875.

32. Egger, S.M., Hurley, K.R., Datt, A., Swindlehurst, G. & Haynes, C.L. (2015). Ultraporous mesostructured silica nanoparticles. *Chem. Mat.* 27(9), 3193–3196. DOI: 10.1021/cm504448u.

33. Tran, N.M., Nam, Y. & Yoo, H. (2022). Fabrication of dendritic fibrous silica nanolayer on optimized water-glass-based synthetic nanosilica from rice husk ash. *Ceram. Int.* 48(21), 32409–32417. DOI: 10.1016/j.ceramint.2022.07.184.

34. Sagar, T.V., Rao, T.S. & Naidu, K.C.B. (2020). Effect of calcination temperature on optical, magnetic and dielectric properties of Sol-Gel synthesized $Ni_{0.2}Mg_{0.8-x}Zn_xFe_2O_4$ (x = 0.0–0.8). *Ceram. Int.* 46(8, Part B), 11515–11529. DOI: 10.1016/j.ceramint.2020.01.178.

35. Luo, D., Yuan, J., Zhou, J., Zou, M., Xi, R., Qin, Y., Shen, Q., Hu, S., Xu, J., Nie, M., Xu, D. & Wu, B. (2021). Synthesis of samarium doped ferrite and its enhanced photocatalytic degradation of perfluorooctanoic acid (PFOA). *Opt. Mater.* 122, 111636. DOI: 10.1016/j.optmat.2021.111636.

36. Sadeghzadeh-Attar, A. (2018). Efficient photocatalytic degradation of methylene blue dye by SnO_2 nanotubes synthesized at different calcination temperatures. *Sol. Energy Mater. Sol. Cells* 183, 16–24. DOI: 10.1016/j.solmat.2018.03.046.